Publication Year	2013
Acceptance in OA@INAF	2024-02-07T10:34:18Z
Title	Mars ionosphere total electron content analysis from MARSIS subsurface data
Authors	CARTACCI, MARCO; Amata, E.; CICCHETTI, ANDREA; NOSCHESE, RAFFAELLA; GIUPPI, Stefano; et al.
DOI	10.1016/j.icarus.2012.12.011
Handle	http://hdl.handle.net/20.500.12386/34717
Journal	ICARUS
Number	223

Mars ionosphere total electron content analysis from MARSIS subsurface data

M. Cartacci[1*], E. Amata[1], A. Cicchetti[1], R. Noschese[1],
S. Giuppi[1], B. Langlais[2], A. Frigeri[1], R. Orosei[1], G. Picardi[3]

[1]Istituto di Astrofisica e Planetologia Spaziali (IAPS), Istituto Nazionale di Astrofisica (INAF), Rome, Italy.

[2]Laboratoire de Planétologie et Géodynamique de Nantes, CNRS and University of Nantes, France

[3]Dipartimento di Ingegneria dell'Informazione, Elettronica e Telecomunicazioni (DIET), Università "Sapienza", Rome, Italy.

*Corresponding author. Fax: +39 06 4993 4383

E-mail address: marco.cartacci@iaps.inaf.it (M. Cartacci, Rome, Italy)

ermanno.amata@ifsi-roma.inaf.it (Ermanno Amata, Rome, Italy)

andrea.cicchetti@iaps.inaf.it (Andrea Cicchetti, Rome, Italy)

raffaella.noschese@iaps.inaf.it (Raffaella Noschese, Rome, Italy)

stefano.giuppi@iaps.inaf.it (Stefano Giuppi, Rome, Italy)

benoit.langlais@univ-nantes.fr (Benoit Langlais, Nantes, France)

alessandro.frigeri@iaps.inaf.it (Alessandro Frigeri, Rome, Italy)

roberto.orosei@iaps.inaf.it (Roberto Orosei, Rome, Italy)

ABSTRACT

We describe a method to estimate the Total Electron Content (TEC) of the Mars ionosphere from the output parameters of an algorithm, called the Contrast Method (Picardi et al. 2000, Ilyushin and Kunitsyn 2004), which allows to correct the phase distortion of the echoes recorded by the Mars Advanced Radar for Subsurface and Ionosphere Sounding (MARSIS) (Picardi et al. 2005) in its subsurface mode. Based on the TEC values evaluated during 6 years of MARSIS activity, corresponding to about 4600 orbits, in this paper we present a global map of the night side TEC variations, which correlates well with the magnetic field model derived from MGS (Mars Global Surveyor) Magnetometer/Electron Reflectometer (MAG/ER) data. In particular, we demonstrate that regions of enhanced TEC preferentially correspond to areas where crustal magnetic field lines are quasi perpendicular to the Martian surface; moreover, we demonstrate that, in regions where the magnetic field is predominantly nearly vertical, enhanced TEC values correlate with higher field intensities, while in regions where the magnetic field is predominantly nearly horizontal, such correlation is not observed. As already suggested in the past by other authors, we suggest that increased TEC values may be related to the precipitation of electrons from the Martian magnetospheric tail along vertical crustal magnetic field lines.

1. Introduction

It is well known that the day side ionosphere of Mars is very different from its night side counterpart. The first obvious difference resides in the fact that the day side is directly hit by solar EUV photons which ionize atmospheric neutrals; moreover, many different factors, external and internal, are at play. As regards the day side, other factors add to photo-ionization: solar cycle, solar rotation, solar flares, cosmic rays, gamma ray bursts etc. (Lillis et al., 2009). As for the night side, the main factors are: neutral density, day-night plasma transport, recombination rates etc. (Lillis et al., 2009) .

An important fact regarding the Martian ionosphere is that, by contrast to Earth, which has a strong geomagnetic field of core origin, Mars does not possess an appreciable global magnetic field. In these conditions, the solar wind can directly interact with the Martian ionosphere and induce modifications of its local properties. However, the magnetometer carried by the MGS mission has established that the planet has strong (up to 1600 nT at ~90 km of altitude) local magnetic fields, related to properties of the Martian crust (Acuna et al., 1999; Nielsen et al. 2006). Such crustal magnetic field lines close in the lower ionosphere and the associated magnetic perturbations are also detected in the upper ionosphere. Magnetic field intensities exceeding 200 nT were measured around 400 km above the surface, but in some regions this influence extends up to 700 Km (Langlais et al., 2010). The combination of the complicated topology of crustal magnetic field with the various factors influencing ionospheric conditions can produce some areas where the ionization is higher and the recombination is lower, producing high values of the electron density even on the night side (Safaeinili et al., 2007).

The night side ionosphere has been the object of various investigations, although its full comprehension is still far from complete (see, e.g. Lillis et al., 2011, and Withers, 2009).

Using MARSIS AIS observations, which only respond to the top side ionosphere, Gurnett et al. (2008) found that, for solar zenith angles (SZA) exceeding 100°, the ionosphere displayed “irregular patches”, more dense where the magnetic field is more intense, while Němec et al. (2010) found AIS ionospheric echoes in ~9% of cases for SZA > 107° and analyzed nightside MARSIS airborne imaging spectrometer data, so as to find 90 cases of ionospheric echoes with SZA > 125°, all in regions of open magnetic field and with higher peak electron densities corresponding to stronger magnetic fields. Complementing these observations, Leblanc et al. (2008) showed a case study where three simultaneous observations were correlated: TEC increase, increase of the flux of precipitating electrons, and observation of a nightside UV aurora. Moreover, for SZA > 100°, Safaeinili et al. (2007) showed that the Total Electron Content (TEC) is higher where the local magnetic field is nearly vertical, while Lillis et al. (2010) showed that during solar particle events TEC increases by more than a factor of 2 may take place.

In this paper, we present a night side map of TEC variations (ΔTEC) based on data collected by MARSIS in its subsurface operation mode. Being based on data collected during 4600 orbits, this map provides a more complete coverage of the planet and is based on a larger statistics than the previous similar map by Safaenili et al. (2007). We show that higher concentrations of ΔTEC are observed at locations where the ionospheric magnetic field is nearly vertical and suggest that, when such a correlation exists, the magnetic field intensity is high; on the contrary, lower concentration of TEC are observed at locations where the magnetic field is roughly horizontal and has a low intensity.

Section 2 recalls the main facts about MARSIS; section 3 contains a brief description of the main effects of the Martian ionosphere on radar propagation; section 4 shows how TEC can be calculated through the "Contrast Method" and discusses the choice of concentrating on the night side leg of the orbits; section 5 compares the night side ΔTEC map with an MGS magnetic field map; section 6 contains a discussion of the results in relation with previous works, a brief summary and some hints on possible future developments. The Appendix provides a description of the Contrast Method, which has the main goal of compensating the distortions of the MARSIS subsurface data caused by the Martian ionosphere.

2. **The MARSIS instrument**

The Mars Advanced Radar for Subsurface and Ionosphere Sounding (MARSIS) (Picardi et al. 2005) is a nadir-looking pulse limited radar sounder, which uses synthetic aperture (SAR) techniques and is carried by ESA's Mars Express spacecraft. MARSIS has the main task of evidencing the presence of water, both liquid and solid, on Mars, with the secondary objective of characterizing the structure of the Martian ionosphere. Therefore, the MARSIS design has foreseen two operation modes: the SS (Sub-Surface) Mode and the AIS (Active Ionosphere Sounding) Mode.

In its SS mode, MARSIS transmits radar pulses that penetrate through the planetary surface and are reflected by any dielectric discontinuity in the subsurface. MARSIS pulses consist of "chirps", i.e. wave packets of duration T = 250 μsec, which are linearly modulated in frequency over a bandwidth B = 1MHz about a central frequency. The latter can be chosen between 4 different values (1.8, 3, 4 and 5 MHz), according to the predicted SEA, so that the chirp frequency is always higher than the local plasma frequency. Under such conditions, the free-space spatial resolution after the so-called "range compression" (which is defined as the convolution between the received chirp signal and a reference function representing the emitted chirp) is approximately 150 m, which corresponds to 50-100 m in the subsurface, depending on the real dielectric constant value of the subsurface layers. The SAR processing is designed so as to obtain synthetic apertures (called frames) adjacent to each other, with a ground resolution of 5.5-10 km along the track and of 17-30 km across the track, where lower and higher resolutions pertain to higher and lower S/C altitudes, respectively. The receiving window duration is 350 μs and the sampling frequency is f_s = 1.4MHz, so that each frame contains 490 samples that increase to 512 after zero padding and FFT processing. During the same SAR, MARSIS usually alternates two frequencies at PRF (Pulse Repetition Frequency) steps, so as to increase the probability that at least one of them propagates above the plasma frequency: the higher frequency (F01) is emitted before the lower one (F02). One additional feature of MARSIS is that it is equipped with a tracking loop that allows the radar to keep echoes within the receiving window regardless of the presence of any additional ionospheric delay.

As the penetration depth of radar signals in the subsurface is approximately proportional to their wavelength (with the exception of ice), MARSIS operates at the lowest possible frequencies capable of propagating through the Martian ionosphere, i.e. just above the local plasma frequency, f_p. As the electron density is known to be definitely lower in the night side, this constraint implies that the MARSIS subsurface sounder is best utilized for negative values of the SEA (Sun Elevation Angle, i.e. the angle between the direction of the geometric centre of the Sun's apparent disk and the horizon). However, as the ionospheric layer extends between 100 and 200 km, the true night side is usually considered to correspond to SEA < -20° /-15°, so that the Sun light cannot reach the ionosphere at all.

3. **The effects of the Martian ionosphere on MARSIS signal propagation**

The propagation of an electromagnetic wave of frequency f in the Martian ionosphere is characterized by the following refraction index

$$n(z) = \sqrt{1 - \frac{f_p^2(z)}{f^2 - jf\nu}} \cong \sqrt{1 - \frac{f_p^2(z)}{f^2}} \qquad (1)$$

where f_p is the plasma frequency, ν the electron-neutral collision frequency and z is the altitude above ground. If we consider a typical MARSIS operation frequency (i.e. in the 1.3-5.5 MHz range), the imaginary term in the denominator of Eq. (1) can be neglected, because $\nu \sim 10 - 60$ kHz. The plasma frequency, in Hz, can be written as

$$f_p(z) = 8.98\sqrt{N_e(z)}, \qquad (2)$$

where N_e is the electron density in m^{-3}. The maximum value of f_p obviously corresponds to the maximum value of the electron density N_{emax}.

As a consequence of Eq. (1) all frequencies lower than f_p will be reflected regardless of the incidence angle. Moreover, if the radar signal has a wide band, the propagation speed is not constant through the band and a frequency dependent phase shift arises. In other words, frequencies higher than f_p will be attenuated, delayed by an average delay (group delay) in signal travel time and dispersed depending on the electron density values encountered along the path.

The phase shift induced by the ionosphere in a radar signal of frequency f can be written as

$$\Delta\phi(f) = \frac{4\pi}{c} f \int_0^L [n(z) - 1]dz = \frac{4\pi}{c} f \int_0^L \left[\sqrt{1 - \left(\frac{f_p(z)}{f} \right)^2} - 1 \right] dz, \qquad (3)$$

where L is the ionosphere thickness and c is the speed of light in vacuum.

If f_0 is the central frequency of the radar signal band, we can perform a Taylor expansion of the integrand of Eq. (3) and then integrate each term of the expansion, so as to obtain

$$\Delta\phi(f) \cong a_0 + a_1(f - f_0) + a_2(f - f_0)^2 + a_3(f - f_0)^3 + a_4(f - f_0)^4 + \ldots, \qquad (4)$$

where:

$$a_0 = \frac{4\pi}{c}\int_0^L \left(\sqrt{f_0^2 - f_p^2} - f_0\right)dz \quad [rad]$$

$$a_1 = \frac{4\pi}{c}\int_0^L \left(\frac{f_0}{\sqrt{f_0^2 - f_p^2}} - 1\right)dz \quad [rad / Hz]$$

$$a_2 = -\frac{4\pi}{c}\int_0^L \left(\frac{f_p^2}{2(f_0^2 - f_p^2)^{\frac{3}{2}}}\right)dz \qquad [rad / Hz^2] \qquad (5)$$

$$a_3 = \frac{4\pi}{c}\int_0^L \left(\frac{f_0 f_p^2}{2(f_0^2 - f_p^2)^{\frac{5}{2}}}\right)dz \quad [rad / Hz^3]$$

$$a_4 = \frac{4\pi}{c}\int_0^L \left(\frac{4 f_0^2 f_p^2 + f_p^4}{8\left(f_0^2 - f_p^2\right)^{\frac{7}{2}}}\right)dz \quad \left[rad / Hz^4\right]$$

The effect of the $a_0, \ldots, a_4$ expansion coefficients on the MARSIS SS performance can be briefly described by recalling that the SS data are processed through the range compression. In the case of a perfect reflection at the Martian surface and of propagation in free space, the range compression would yield a time dependent signal power characterized by a central lobe and a number of side lobes (as a consequence of the linear variation of the frequency within the chirp). After range compression, the theoretical main lobe width should be 1 μsec wide, while the difference in power between the main lobe peak and the first side lobe peak should be 32 dB. These parameters characterize the radar range resolution, that is the ability to reveal objects close to one another, and the radar dynamic range, which affects the capability to detect subsurface echoes.

Fig. 1 displays the range compression of the ideal reflected signal (i.e. in free space - blue line) and the range compressions pertaining to the a_1, a_2, a_3, and a_4 expansion terms (blue dotted, black, red and purple lines, respectively), all evaluated through the simplified expressions given in Eqs. (A.11) of the Appendix, assuming that f_p = 1 MHz and τ_0 = 533 μs. All lines have been normalized to their peak values. We notice that the a_1 term only introduces a time shift (group delay), while the higher terms yield phase distortions. In particular, the a_4 term smears out the side lobes, while the a_3 term enhances the lobes preceding the main lobe and reduces those following it. The most relevant effect is that due to the a_2 term, which seriously affects the received chirp slope.

In conclusion, we see that the ionosphere can severely degrade the data quality, i.e. increase the side lobe levels, distort the waveform shape, and worsen the signal to noise ratio and range resolution. Moreover, the MARSIS signal is very vulnerable to ionosphere effects especially in those areas where the ionosphere and the magnetic field effects are combined together, because in these areas distortions are larger than usual. Obviously all the effects will increase steadily passing from the night side to the day side.

Due to the relevance of this topic for the mission success, different methods have been proposed to correct the ionosphere distortion.

Ilyushin and Kunitsyn (2004) described various methods, including a theoretical reconstruction of the signal phase, starting from its spectrum, with the use of an error function and a polynomial regression. Safaeinili et al. (2003) and Mouginot et al. (2008) proposed a recursive method to optimize the SNR with a phase correction term, considering the constraint that the measured phase after correction must be coincident with the phase obtained from the signal travel time expected from MGS-MOLA data; moreover, in order to initialize their recursive algorithm, they used a Gaussian approximation of the dependence of electron density on altitude. The core of the method used by Zhang et al. (2009) is a recursive loop to search for the best electron density N_e and electron-neutral collision frequency, neglected in Eq. (1), which optimize the SNR .

The study presented in this paper is based on the Contrast Method, CM hereafter, which is briefly described in the Appendix.

4. **Evaluation of TEC through the Contrast Method**

4.1 TEC evaluated through the CM

We show in the Appendix that, when MARSIS is probing the subsurface, the CM provides an estimate of a_2 for each SAR.

In the night side, usually $f_p \leq 1$ MHz, so that, excluding the lowest MARSIS SS frequency of 1.8 MHz, we have $f_p^2/f_0^2 << 1$. Therefore, we can approximate the a_2 parameter of Eq. (5) as

$$a_2 \cong -\frac{4\pi}{c}\int_0^L \frac{1}{2}\frac{f_p^2}{f_0^3}\,dz = -\frac{2\pi}{c\,f_0^3}\,(8.98)^2\int_0^L N_e\,dz \qquad (6)$$

by keeping only the first term of the series expansion of the function $f_p^2/(f_0^2 - f_p^2)^{3/2}$, i.e. by neglecting a $-\frac{3\pi}{c\,f_0^5}\,(8.98)^4\int_0^L N_e^2 dz$ term. This approximation yields an overestimate of the absolute value of a_2 of the order of $1.5(f_p/f_0)^2$, which, for f_p=1 MHz and f_0= 4 MHz, is about 10%. The inversion of Eq. (6) allows us to write

$$TEC \cong -\frac{a_2 c\,f_0^3}{2\pi(8.98)^2} \qquad (7)$$

where $TEC = \int_0^L N_e\,dz$ is the total electron content of the ionosphere, with the caveat that the calculation through Eq. (7) always implies an overestimate of the TEC. In practice, as our study will be limited to SEA < 0° and to f_0= 4 MHz (see the summary of this section), this overestimate will at generally be lower than 10% (but it can at times be higher for negative values of SEA close to 0°). In Section 5 we will further comment on this issue.. The correction of this error could be the subject of a future study.

4.2 TEC filtering and validation

The use of the CM over the whole MARSIS dataset has produced millions of TEC estimates for different conditions of solar zenith angle, latitude and longitude. As an example, Fig. 2a shows TEC values, as a function of the SEA, along orbit 6001, calculated from radar signals at frequencies of 3, 4 and 5 MHz (red, blue and black lines, respectively). The three lines are in good agreement, but at times they appear to be rather noisy, as many large spikes and fluctuations are superimposed to the general increase of TEC. This suggests that, before proceeding further, a filtering process should be applied to the TEC evaluated from Eq. (7). Fig. 2b displays the same data after spikes have been removed and a low pass filter (a zero-phase digital filter that processes the input data in both the forward and reverse directions) has been applied to them; hereafter, we call the result of such a process TEC_{filt}. We notice that in the night side (for SEA < -25°) the 3 and 4 MHz lines roughly coincide. The residual differences between the two lines in that region could be due to various transient effects whose relative influences are difficult to establish quantitatively (different number of echoes collected at different frequencies, frequency dependent surface and subsurface effects, frequency dependent transmitter distortions and antenna performance). We also remark that in the range -16°< SEA < 0° the 3 MHz TEC is generally slightly higher than the 4 MHz one. A straightforward interpretation of this result is that in that region, as the day side is approached, the plasma density increases, so that the condition $(f_p / f_0)^2 << 1$ starts to break down: when that happens, the value of a_2 provided by the CM is overestimated, which in turn leads to a TEC value larger than it should be. Similarly, in the day side the 4 MHz TEC is usually larger than the 5 MHz TEC.

Before proceeding further, we compared the TEC_{filt}, obtained in the 4 MHz mode, with the TEC calculated by Mouginot et al. (2008). Figs. 3 and 4 show the comparison between the two TECs for orbits 2600 and 2640, respectively, for negative SEA values only (because, as we argue further on, the study described in this paper is focused on the night side). The TEC estimated through the Mouginot et al. (2008) method, red dotted line, has been filtered in the same way as TEC_{filt}, blue dotted line. Figs. 3 and 4 demonstrate that in the night side the two TECs generally agree and display similar fluctuations and trends.

TEC_{filt} values were calculated from 4600 orbits between July 2005 and October 2011. In order to test such a large dataset for consistency, we first of all calculated averages of TEC_{filt} in 0.1° SEA bins for all four available frequency bands. Fig. 5 displays such averages of TEC_{filt} as a function of SEA for the four frequencies and shows that TEC_{filt} clearly and steadily increases as the SEA passes from negative (night side) to positive (day side) values.

Fig. 5 shows that, in the night side, the average TEC_{filt} values, estimated for the four different frequencies, coincide, exception made for some residual peaks which seem to occur mainly for 4 MHz TEC_{filt} values. However, as the SEA increases and the transmitted frequency approaches the local plasma frequency, the scatter of TEC_{filt} values above or below the average trend increases. This means that, under such conditions, TEC_{filt} suffers from a loss of accuracy, because the quadratic term estimated through the CM is not sufficient to fully compensate the distortion caused by the ionosphere. At 1.8 MHz the plasma frequency is already approached at about -20°. In fact, we see that, for SEA > -20°, the velvet points in Fig. 5 deviate from the general trend. Consequently, above -15°we did not plot 1.8 MHz TEC_{filt} values. Similarly, we did not plot 3 MHz TEC_{filt} values above 0°. f_0=4 MHz is the only MARSIS operation frequency that produces a complete data set covering both the night and the day side; on the other hand, f_0=5MHz provides data over the whole day side.

The blue solid curve of Fig. 5 displays the TEC evaluated through the Chapman model (Chapman, 1931). The electron density of the Chapman model is

$$n_e\left(\frac{h-h_0}{H},\chi\right)=n_0\exp\left(-0.5\left(1-\frac{h-h_0}{H}-Ch\left(\frac{R+h}{H},\chi\right)\exp\left(-\frac{h-h_0}{H}\right)\right)\right) \quad (8)$$

where h_0 is the altitude of the maximum electron density, H is the neutral scale height and Ch is the Chapman incidence function

$$Ch\left(\frac{R+h}{H},\chi\right)=\frac{R+h}{H}\sin\chi\int_0^{\chi}\exp\left(\frac{R+h}{H}-\frac{R+h}{H}\frac{\sin\chi}{\sin\alpha}\right)\mathrm{cosec}^2(\alpha)\,d\alpha \quad (9)$$

In Fig. 5 the Chapman model has been evaluated with the following parameters: $n_0 = 2.2*10^{11}$ m^{-3}, $h_0 = 130*10^3$ m, $H = 13*10^3$ m, chosen so as to obtain an overall acceptable fit of the experimental data. Given the nature of the Chapman model, a comparison with the experimental TEC only makes sense for SEA > -10°. From Fig. 5 it is clear that the experimental 4 MHz TEC_{filt} values and the theoretical model match quite closely over a 10°-20° interval roughly centered at SEA = 0°, while they differ on the day-side, above 10°, where the model forecasts first lower, then higher values than the observed TEC_{filt}. As regards the 5 MHz TEC_{filt} values, we notice that they practically coincide with the 4 MHz ones close to SEA = 0°, while they better agree with the model in the 10°-20° range and start deviating considerably from the model around 25°, where the plasma frequency becomes too high for the CM to produce a reliable TEC estimate.

4.3 Solar activity effects on TEC

The averages displayed in Fig. 5 have been obtained over a period of several years. As a consequence, all possible effects due to variations of solar activity have been probably smoothed in the averaging process. However, it is expected that the solar activity can severely degrade the radar signal propagation, mainly because of solar flares (Espley et al. 2007). Therefore, in order to briefly study the behavior of TEC_{filt} under different solar conditions, we have conducted the same analysis used for generating Fig.5 after having grouped the data according to the year. Fig. 6 shows averages of 4 MHz TEC_{filt}, calculated over 0.1° SEA bins and plotted as a function of SEA, for five subsequent years. Figs. 6a and 6b pertain to the night and to the day side, respectively, and have different ordinate scales due to the large excursion of TEC_{filt} from night to day. As regards Fig. 6a, we see that the scatter of points around the average trends is of the order of 0.1-0.2 10^{15} m^{-3} for each year; however, the TEC_{filt} values pertaining to the five years become more and more different as the SEA increases towards the day side, although the largest difference is roughly 0.5 10^{15} m^{-3} for values pertaining to 2007 and 2008. In the Fig. 6b, we clearly see that the average TEC_{filt} values are very different in different years; moreover, the dependence on the SEA varies a lot from year to year. These results suggest that, for every statistical analysis conducted on data pertaining to distinct years, these differences must be properly taken into account.

4.4 Section summary

To conclude this section, we summarize hereafter its main findings.

- TEC can be calculated through the Contrast Method. However, its values are generally overestimated by a factor $1.5(f_p/f_0)^2$. For f_0 = 4MHz and f_p = 1MHz, this corresponds to 10%, but it can attain larger values as SEA approaches 0° from the night side.
- The Martian TEC seems to depend on solar activity. This dependence shows up as a shift of TEC to higher or lower values over the entire SEA range, as a function of the year in the solar cycle.
- The overall dependence of the Chapman model TEC on SEA is in good agreement with the experimental TEC data for SEA>-10°, provided that the chirp frequency is well above the local plasma frequency.
- When the plasma frequency gets too close to the chirp frequency, TEC values display large deviations from the average TEC trend and from the Chapman model.
- The best chirp central frequency for the calculation of TEC in the night side is f_0 = 4MHz, as confirmed by the comparison of the CM TEC with the Mouginot et al. (2008) TEC.

5. **MARSIS TEC variations in relation to the Martian crustal magnetic field**

5.1. General considerations

The conclusions drawn at the end of the preceding section clearly suggest that the day side data must be treated with great care, while the night side TEC data can be used to build a map of TEC covering most of the planet. Safaeinili et al. (2007) calculated for each orbit the per cent variations of TEC relative to the average night side TEC, displayed such per cent variations through a longitude-latitude map and compared it with a map of the crustal magnetic field, suggesting that at times a correlation existed between the two. However, the map obtained by Safaeinili et al. (2007), which was based on only 750 orbits and included only data from portions of the orbit for which SEA < -10°, did not fully cover all latitudes and longitudes. Based on our larger data base, we aim at increasing as much as possible the longitude-latitude coverage of such a map. However, as also in our case the SEA < -10° restriction does not allow us to obtain a continuous coverage, we have devised an improved method to derive reliable per cent variations of TEC also for SEA values comprised between -10° and 0°.

5.2. Calculation of TEC variations

The principle of our method can be easily explained by considering Fig. 7, in which the blue curve displays TEC_{filt} values in the (-30°,13°) SEA range for orbit 6001 and f_0=4 MHz. We notice that, between -32° and-15°/-10°, TEC_{filt} undergoes several humps and hollows, while it oscillates around a night time average value of about 0.3 10^{12} m^{-2}. As SEA increases from -15°/-10° to 13°, TEC_{filt} displays a clear positive trend over which other small oscillations are superimposed. Therefore, it makes sense to calculate ΔTEC with respect to the night time average value, as done by Safaeinili et al. (2007), only up to -10° of SEA, while the extension of such a calculation to the whole SEA range of Fig. 7 or even just to the (-15°,0°) range would undoubtedly yield unreasonable results, as the new average would be much higher.

We fitted the TEC_{filt} values with a 10^{th} order polynomial, plotted in purple in Fig. 7, and calculated ΔTEC as the difference between TEC_{filt} and the fit function, as shown by the black curve in Fig. 7. A caveat must be added at this point: as discussed in Section 4, our evaluation of TEC (see eq. 7) is affected by a systematic error, which yields an overestimate of TEC roughly proportional to the TEC itself through a f_p^2/f_0^2 factor. As a consequence, a similar overestimate could show up in ΔTEC. In practice, however, we see from Fig. 7 that the absolute value of ΔTEC does not significantly increase between SEA = -10° and SEA = 0°, so that we obtain reasonable values of ΔTEC for all negative SEAs. In fact, deviations from the fit function show up along the whole orbit as humps or hollows with amplitudes up to 0.5 10^{15} m^{-2} which occur over orbital distances corresponding to SEA excursions ranging from 2°-3°to 5-7°. All other orbits show similar behaviors, although the locations and amplitudes of humps and hollows vary from one orbit to the other. It is interesting to remark that ΔTEC is generally much smaller than the corresponding fit function value, but it can be at times of the order of the fit function for negative values of the SEA.

The definition of ΔTEC and of TEC_{filt} allows in principle to generalize the calculation of the per cent ΔTEC relative to the fit function, i.e. to define $\Delta TEC_{pc}=100(\Delta TEC/TEC_{filt})$ for any value of SEA. However, Fig. 7 clearly suggest that a given absolute value of ΔTEC can be of the order of even larger than the corresponding TEC_{filt} value deep in the night side, while it will result to be considerably smaller than the corresponding TEC_{filt} value in the day side. As a consequence, it does not make sense to calculate ΔTEC_{pc} in the day side and we limit such a calculation to negative values of SEA, thus including the -15°<SEA<0° interval. This new definition of ΔTEC_{pc} yields an increase of the available ΔTEC_{pc} values by 27%, which allows, as we will see in the following, to build a map covering all longitudes and all latitudes below 54° (above 54° the map cannot be built due to the fact that in the nightside MARSIS data over that region are too sparse).

Having made this choice, as a next step in our analysis, we excluded all the day side data, that is those for which SEA>0°, and then computed ΔTEC_{pc}, point by point and for each orbit.

5.3. *Maps of ΔTEC_{pc} and of magnetic field inclination*

We binned all the night side ΔTEC_{pc} in a grid with 0.5° resolution, from -90° up to +54° geographical latitude and covering all geographical longitudes, averaging the data collected in each bin. The resulting two dimensional matrix of percentages has been two-dimensionally low pass filtered, in order to further reduce noise and then interpolated to achieve a resolution of 0.25° and improve the quality of the maps. Fig. 8 shows the latitude-longitude map of the final ΔTEC_{pc}. The data have been coded according to the scale displayed on the right, which has been chosen so, that it is possible to appreciate both the spatial structure of ΔTEC_{pc} and the distribution of ΔTEC_{pc} values. ΔTEC_{pc} values mostly fall between -20% and +20%, but large positive and negative values are also seen, as expected from the ΔTEC plot shown in Fig. 7 for orbit 6001. On the other hand, we also notice that spatial structures are exhibited by ΔTEC_{pc}, similarly to what was earlier observed by Safaeinili et al. (2007), who suggested a dependence of their ΔTEC_{pc} on the orientation of the crustal magnetic field (in this regard, see their Figs. 3a and 3b).

In order to enhance the spatial structures exhibited by ΔTEC_{pc}, Fig. 9a shows the same ΔTEC_{pc} values as shown in Fig. 8, plotted according to the new scale shown on the right. The effect of the new scale is that positive values of ΔTEC_{pc} appear as whitish spots, while negative values appear as blackish spots. Fig. 9b displays the corresponding latitude-longitude maps of the angle (which we hereafter call α) between the ambient magnetic field vector at 200 km above the mean spherical radius and the local vertical direction (taking α to be positive for both upward and downward field). This angle has been computed from magnetic field predictions at a constant altitude from an

Equivalent Source Dipole model (ESD), based on the approach used by Langlais et al. (2004) and updated to account for more recent measurements. This new model uses magnetometer (MAG) actual rather than geographically averaged measurements of the three magnetic field components, acquired during all the phases of the MGS mission. The MAG data selection scheme was improved in order to eliminate most of the transient, time-varying, magnetic field contributions. The ESD mesh consists of a grid of 10,602 locations, with a mean spacing of 1.97° (117 km along the Martian equator). This new model therefore relies on more measurements, with an increased altitude coverage, with less contaminating external fields entering and a better lateral resolution. The constant-altitude map is computed with a 0.25° resolution both in latitude and in longitude. Areas where the field is quasi-horizontal, or with values of α close to 90°, are coded in black, while areas corresponding to a quasi-vertical field, with values of α close to 0°, are coded in white.

A careful examination of Fig. 9 suggests that regions of quasi-vertical magnetic field often correspond to regions of positive ΔTEC_{pc}, while regions of quasi-horizontal magnetic field often correspond to regions of negative ΔTEC_{pc}. In order to highlight this, we drew two dashed lines in the lower panel: the red one along an extended region of vertical magnetic field; the yellow one along a region of horizontal field. We then copied the two lines onto the upper panel at exactly the same longitudes and latitudes. We see that, in the highlighted regions, the correlation between magnetic field orientation and ΔTEC_{pc} is strikingly good. On the other hand, it must be also remarked that in other regions of Fig. 9 the correlation between vertical (horizontal) field and high (low) ΔTEC_{pc} is blurred or not seen at all.

A region where the correlation between the field direction and ΔTEC_{pc} appears to be particularly good is evidenced in Fig. 10, which shows blow-ups of the α and ΔTEC_{pc} maps between -64° and -7° in latitude and 104° and 194° in longitude. Again we highlight the vertical field and high ΔTEC_{pc}

through red dotted lines and the horizontal field and low ΔTEC_{pc} through yellow dashed lines. Further on in the text, we will refer to this region as to region 1 (R1 for short).

5.4. Analysis of ΔTEC_{pc} in relation to magnetic field inclination and intensity

The comparison between the maps of α and ΔTEC_{pc} deserves further investigation, in order to quantitatively estimate the similarity of the structures which are present in each of them. Here we add some statistical analysis to perform a first order quantitative assessment. The results of this analysis are displayed in Fig. 11. First of all, we considered two subsets of the whole ΔTEC_{pc} map, the first comprising of all 1°x1° pixels for which $0^\circ<\alpha<10^\circ$ (corresponding to nearly vertical magnetic field), the second comprising of all 1°x1° pixels for which $80^\circ<\alpha<90^\circ$ (i.e. nearly horizontal field). Panel a of Fig. 11 displays the histograms of the ΔTEC_{pc} values pertaining to the $0^\circ<\alpha<10^\circ$ subset (black solid cityscape) and to the $80^\circ<\alpha<90^\circ$ subset (dotted cityscape), as a function of ΔTEC_{pc} , in 40 bins between -100 and 100. Each histogram has been normalized to its peak value, being the peak value 278 for the $0^\circ<\alpha<10^\circ$ histogram and 1793 for the $80^\circ<\alpha<90^\circ$ histogram. First of all, we notice that in the vast majority of cases ΔTEC_{pc} is observed to fall between -20 and 20, which is agreement with the distribution of values indicated by the grey scale coding in Fig. 8. The histogram pertaining to the $80^\circ<\alpha<90^\circ$ subset has its peak in the (-5,0) bin and is nearly symmetrical with respect to 0. We also examined the histogram of all ΔTEC_{pc} values displayed in Fig. 8, but, as we found that it is rather similar to the $80^\circ<\alpha<90^\circ$ one, we do not show it in order not to overload panel a. Moving to the histogram pertaining to the $0^\circ<\alpha<10^\circ$ subset (black solid cityscape), we notice that it differs from the first one, as the dotted cityscape is steadily and consistently above the black solid cityscape for negative values of ΔTEC_{pc}; on the contrary, the quasi-vertical field histogram is steadily higher than the quasi-horizontal one for positive values of

ΔTEC_{pc}. Moreover, its peak is shifted to the (0,5) bin. In conclusion, we may state that panel a of Fig.11 confirms the consideration we made concerning Fig. 9, insofar as regions of quasi-vertical magnetic field preferentially correspond to regions of positive and high positive ΔTEC_{pc}, while regions of quasi-horizontal magnetic field preferentially correspond to regions of negative ΔTEC_{pc}. The correlations between quasi vertical magnetic field and positive ΔTEC_{pc} on one side, and between quasi horizontal magnetic field and negative ΔTEC_{pc} on the other side, are further highlighted in panel b of Fig. 11, which displays the histograms for quasi vertical magnetic field (solid cityscape) and quasi horizontal magnetic field (dotted cityscape) for the region 1 highlighted in Fig. 10. We remark that in panel b the histogram pertaining to the quasi-vertical magnetic field is further shifted towards positive values of ΔTEC_{pc}, while the one for quasi-horizontal field is shifted in the opposite direction: quantitatively, we find that for quasi-vertical magnetic field, 70% of the 1°x1° bins display a positive ΔTEC_{pc} value, while 75% of the bins corresponding to a quasi-horizontal field display a negative ΔTEC_{pc} value.

In Fig. 9 several regions can be seen where the correlation between ΔTEC_{pc} and α seems not to hold. One such a region, to which we will hereafter refer as region 2 (R2 for short) extends between 5° and 25° in latitude and between 130° and 190° in longitude. Panel c of Fig. 11 displays, for R2, similar histograms as those of panel b for R1. In panel c it is evident that the two histograms are more similar than those of panel b, apart from some fluctuations which can be ascribed to the smaller extension of the region, which yields a lower statistics. As both R2 and R1 contain quasi vertical and quasi horizontal field orientations, one can look for another physical quantity, e.g. the total magnetic field intensity, which might play a role in relation to the observation of positive or negative values of ΔTEC_{pc}. Panel d displays the histograms of the total magnetic field intensity for R2 (dotted cityscape) and for R1 (solid cityscape). We see that the difference between the two is strikingly clear: practically all R2 bins correspond to a weak total magnetic field, below 50 nT; on the contrary, the R1 histogram displays only a few values below 10 nT and extends to hundreds of nT.

A possible interpretation of the histogram of Fig. 11d is that a higher magnetic field intensity, B, in itself favors high positive values of ΔTEC_{pc}. In order to check this hypothesis, we binned and averaged all ΔTEC_{pc} values of Fig. 8 in 5 nT bins of the corresponding total magnetic field. The lower panel of Fig. 12 displays, as a function of B, such averages of ΔTEC_{pc} (which we call $<\Delta TEC_{pc}>_B$), while the upper panel displays the number of cases pertaining to each 5 nT bin. We see that $<\Delta TEC_{pc}>_B$ is very small for B<20nT, where most of data are concentrated, and exhibits larger positive or negative values for higher and less frequent values of B. The $<\Delta TEC_{pc}>_B$ oscillations are even larger for the few cases of B > 100 nT which we do not show in Fig. 11 due to their irrelevant statistical significance. In conclusion, no prominent dependence of $<\Delta TEC_{pc}>_B$ on B can be inferred from Fig. 12.

In order to further highlight the link between ΔTEC_{pc} and the orientation of the crustal magnetic field, we averaged the ΔTEC_{pc} values of Fig. 8 over 1°x1° pixels and then binned such averages in 5° bins of α by associating each average to the α value pertaining to the given latitude and longitude (according to the α matrix plotted in Fig. 9b) ; finally, 16 averages were calculated (covering the 0°-90° range), which we indicate with $<\Delta TEC_{pc}>_{\alpha}$. Fig. 13 displays, in its lower panel, the plot of $<\Delta TEC_{pc}>_{\alpha}$ as function of α, and, in its upper panel, the plot of the corresponding number of cases. We see that the magnetic field appears to be close to horizontal in the great majority of cases, as $\alpha < 10°$ in only ~1400 out of $5\ 10^4$ cases. However, the bottom panel clearly suggests a dependence on α, as $<\Delta TEC\_pc>_{\alpha}$ is positive (~5%) for quasi vertical field and steadily decreases to negative values (~2%) for quasi horizontal field, being close to 0 for α~45°.

6. Discussion and summary

In this paper we have made use of the Contrast Method, a tool developed to compensate ionospheric distortion effects on radar signals. We have demonstrated that the data collected by the MARSIS radar in its subsurface mode can be processed through the CM, so as to obtain estimates of the nightside TEC of the Martian ionosphere, with the caveat that they can be affected by an overestimate of up to 10%. We have shown that the CM MARSIS TEC values are in good agreement with the predictions of the Chapman model and with similar results described a few years ago iby Safaeinili et al. (2008); moreover, we have shown two examples of good agreement of the CM TEC with the Mouginot at al. (2008) TEC.

As a first application of the CM auxiliary parameter a_2, in this work we calculated TEC values for the Martian ionosphere for all MARS Express orbits from 2006 to 2011: we found that large TEC variations are observed from year to year as far as the day side is concerned. As such variations appear to increase as the SEA increases, it is natural to ascribe them to the evolution with the solar cycle of the conditions on the Sun and in the solar wind. On the contrary, the night side TEC values do not seem to noticeably depend on time on a yearly scale; as a consequence, it has been possible to globally analyze all the night side data and to derive from them maps of TEC as a function of geographical latitude and longitude. For that purpose, we developed a new method of calculating per cent variations of TEC using a 10^{th} order polynomial function and not an average value as done by Safaeinili (2007), which allowed to estimate better the TEC values for -15°<SEA<10°, and to include TEC values for -10°<SEA<0°, so as to achieve a full and continuous coverage of a very large portion of the Martian ionosphere, with the only exclusion of latitudes above 54°. In this regard, our results confirm (see our Figs. 9, 10, 11 and 12), with the support of a much larger data base (i.e. a total of 4600 orbits instead of the 750 orbits considered by Safaeinili et al, 2007), that positive values of ΔTEC are often related to quasi vertical crustal magnetic fields, while negative values of ΔTEC relate to quasi horizontal crustal magnetic fields. Moreover, we found some evidence (see Figs. 11 and 12) that the intensity of the crustal magnetic field also plays a role in connection with the observation of positive ΔTEC values. However, as shown in Fig. 11, the magnetic field intensity alone does not seem to favor the observation of increased TEC values, while we find that a quasi-vertical orientation of the field (see panel d of Fig. 11) favors increases of TEC when the magnetic field intensity is higher than 10-20 nT.

To put the discussion of our results into context, at this point it is useful to recall that several authors noticed in the past (e.g. Nemec et al., 2010 and 2011) the connection between TEC and magnetic field direction. In order to explain it, it is commonly believed that, as the solar wind drapes its frozen-in magnetic field around the planet, a connection might be established between that field and the Martian crustal magnetic fields. Safaeinili et al. (2007) also invoked such a connection, suggesting that it "can result in ionizing of the atmosphere and in the heating of the ionospheric electrons that in turn, slow the recombination process and produce a higher free electron content." On the other hand, other authors observed that higher peak densities tend to occur in the night side in areas of strong crustal magnetic fields. However, the magnetic field strength and topology is only one of the many factors which influence the ionization of the Martian night side ionosphere (e.g. Lillis et al., 2009, list 11 such factors). Still, the results we have shown in the preceding section show that the influence of the crustal magnetic field is clearly detectable. The ΔTEC_pc map that we have obtained (see Figs. 8 and 9a) confirms and strengthens the result of (Safaeinili et al., 2007) about the existence, over extended geographical regions, of a correlation between the orientation of the crustal magnetic field and the observed ΔTEC. In fact, it appears that, in some regions, higher concentrations of TEC are associated with a quasi-vertical magnetic field direction, while TEC depletions are associated with quasi-horizontal field orientations. It must be remarked that such TEC increases and depletions are observed in spite of the fact that data from five years have been averaged together, thus including periods of higher and lower solar activity, as well as periods of quiet and disturbed solar wind conditions. Such a correlation was already suggested by Safaeinili et al. (2007), where it was in particular shown for an individual track along the spacecraft orbit. In this paper we have further studied it following a statistical approach, through histograms of ΔTEC_pc calculated for quasi-vertical and quasi-horizontal local crustal magnetic field line orientations, over the whole ionosphere and over two selected regions, called R1 and R2 in the preceding section. Moreover, we have shown (Fig. 11) that the total intensity of the local magnetic field in general does not play a role in itself in favoring TEC enhancements. Nevertheless, it appears that the magnetic field intensity is important when the field is predominantly nearly vertical. In fact, we have found (cf. panel d of Fig.11) that in R1, where the correlation appears to be more evident than on average (as discussed in relation to panels b and a of Fig. 11, respectively), the magnetic field intensity exceeds in most cases 10-20 nT and attains values of hundreds of nT, while in R2, where the correlation is totally absent (as shown in panel c of Fig. 11), the magnetic field intensity is clearly lower, as it is almost always lower than 50 nT, while its histogram peaks between 5 and 10 nT.

To conclude this discussion and summary, we wish to outline the directions along which we intend to further develop our activities on this matter: 1) investigate a possible dependence of the correlation TEC-magnetic field on conditions in the solar wind and on solar activity; 2) investigate the factors which favor that correlation over some regions only (in this regard, it is probably relevant that the magnetic field is predicted at a constant altitude of 200 km, while the TEC values pertain in general to the 200-400 km interval); 3) further extend the data base, with the objective to fill the northern hemisphere gap (by including the observations of summer 2011 and 2012); 4) extend the study to the day side data; 5) study the lower part of the ionosphere in conjunction with the data obtained with the AIS (Active Ionosphere Sounding) Mode.

Appendix: The Contrast Method

As we have argued in section 3, the MARSIS SS performance is seriously hindered by the signal phase shift due to the Martian ionosphere, in particular by the a_2 term of the Taylor expansion of the phase shift, as shown in Eqs.(4) and (5) and in Fig. 2.

The "Contrast Method" (Picardi et al. 2000) was developed to correct, or at least reduce, the effects due to such a phase shift. In the following, we provide a concise description of the CM.

The CM consists in iterating the range compression of the radar echoes: at each step of the iteration, the following phase compensation is applied to the echoes

$$\Delta\varphi(f) = \hat{a}_2(f - f_0)^2 + \hat{a}_3(f - f_0)^3 + \hat{a}_4(f - f_0)^4 \qquad \text{(A.1)}$$

where the $\hat{a}_2$ term is

$$\hat{a}_2 = \hat{a}_{2\,start} + \left(k - \frac{n}{2}\right)\delta a_2 \qquad 1 \le k \le n \qquad \text{(A.2)}$$

Here n is the number of iterations, $\hat{a}_{2start}$ is the starting value and δa_2 the iteration step. $\hat{a}_{2start}$ is set to zero for the first frame of a given orbit, while for all the following frames it is set equal to the best value of $\hat{a}_2$ estimated in the preceding frame.

In order to estimate an upper value for δa_2, let us define the effect of the ionosphere distortion as:

$$\Phi_1(f) + \Phi_D(f) = \Phi_1'(f) \qquad \text{(A.3)}$$

Where Φ_1(f), Φ_D(f) and Φ'_1(f) are the square-law phase terms of the transmitted signal, of the ionosphere distortion and of the received signal. Considering Eq. (6-20) from Cook and Bernfeld (1967) and Eq. (5), we can write:

$$\Phi_1(f) = \frac{4\pi^2(f - f_0)^2}{2\mu}$$

$$\Phi_D(f) = a_2(f - f_0)^2 \qquad \text{(A.4)}$$

$$\Phi_1'(f) = \frac{4\pi^2(f - f_0)^2}{2\mu'}$$

μ is the slope of the transmitted chirp signal and can be expressed as

$$\mu = \frac{2\pi B}{T} \tag{A.5}$$

where B = 1 MHz and T = 0.25 ms are the chirp bandwidth and duration, respectively, while μ' is the slope of the received chirp.

Eqs. (A.3) and (A.4) yield

$$a_2 = 2\pi^2 \left(\frac{\mu - \mu'}{\mu' \mu}\right) = \frac{2\pi^2 \gamma\prime}{\mu} = \frac{\pi \gamma\prime T}{B} \tag{A.6}$$

where the mismatching factor between transmitted and reflected chirp is

$$\gamma' = \frac{\mu - \mu'}{\mu'} \tag{A.7}$$

We can define the accuracy of the phase correction as:

$$\Delta a_2 = a_2 - \hat{a}_2 = \frac{\pi \gamma' T}{B} - \frac{\pi \hat{\gamma} T}{B} = \frac{\pi T}{B}(\gamma' - \hat{\gamma}) = \frac{\pi T}{B}\gamma \tag{A.8}$$

Where $\hat{a}_2$ and $\hat{\gamma}$ are the estimated correction term and the estimated mismatching factor, respectively, while γ is the residual mismatching factor. From Fig. 6.27, pag. 156 from Cook C.E., Bernfeld M., 1967, we can assume, as a worst case, that:

$$\gamma \leq \frac{2}{BT} \tag{A.9}$$

where B and T are the chirp bandwidth and duration, respectively.

In conclusion, Eqs. A.8 and A.9 yield

$$\Delta a_2 \leq \frac{2\pi}{B^2} = 6.28 \cdot 10^{-12} \quad \text{rad/Hz}^2 \tag{A.10}$$

In practice, in the Eg. (A.2) iteration, it is desirable to use a step smaller than Δa_2. Usually, $\delta a_2 = 0.1\ \Delta a_2$.

In order to determine the $\hat{a}_3$ and $\hat{a}_4$ terms to be used in the iteration defined in Eq. (A.1), we first simplify Eqs. 5 by making use of a model ionosphere characterized by a constant plasma frequency

$f_{p,max}$ and an equivalent slab thickness L_{Eq}. This assumption allows to move the integrand out of the integral, which becomes trivially equal to L_{eq}, so that we obtain

$$a_1 = 2\pi\tau_0\left(\frac{f_0}{\sqrt{f_0^2 - f_{p\max}^2}} - 1\right) \quad [rad / Hz]$$

$$a_2 = -2\pi\tau_0\left(\frac{f_{p\max}^2}{2(f_0^2 - f_{p\max}^2)^{\frac{3}{2}}}\right) \quad [rad / Hz^2] \qquad \text{(A.11)}$$

$$a_3 = 2\pi\tau_0\left(\frac{f_0 f_{p\max}^2}{2(f_0^2 - f_{p\max}^2)^{\frac{5}{2}}}\right) \quad [rad / Hz^3]$$

$$a_4 = -2\pi\tau_0\left(\frac{4 f_0^{\,2} f_{p\max}^2 + f_{p\max}^4}{8\left(f_0^2 - f_{p\max}^2\right)^{\frac{7}{2}}}\right) \quad \left[rad / Hz^4\right]$$

having defined $\tau_0 = 2L_{eq}/c$.

Assuming that $(f_{pmax} / f_0)^2 << 1$, from Eq. (A.11) we easily find that

$$\hat{a}_3 \cong -\frac{\hat{a}_2}{f_o}\left(1 - \frac{\hat{a}_2 f_o}{\pi\tau_o}\right) \qquad \text{(A.12)}$$

$$\hat{a}_4 \cong \left(\frac{\hat{a}_2}{f_0^2}\right)\left(1 - \frac{\hat{a}_2\, f_0}{0.5\pi\,\tau_0}\right)$$

The compensation term Δφ that produces the range compressed signal with the best energy concentration in a defined time interval of the receiving window, is selected to perform the final range compression. In practice, the CM provides $\hat{a}_3$, $\hat{a}_3$ and $\hat{a}_4$ as best estimates of the coefficients of the expansion defined by Eq. (4).

The Contrast Method is applied to all synthetic apertures (frames) collected by MARSIS and for each frequency. Fig. A.1 shows how the CM improves the quality of the range compressed data for a given frame: the red line shows the signal after range compression without correcting the phase through the CM, while the blue line shows it after the CM optimization procedure has been applied.

It is evident that the CM yields a higher peak power, a better signal to noise ratio and a reduction of the main lobe width, leading to a better range resolution; this allows to separate the surface and subsurface echoes that without correction would be merged together.

Acknowledgements

The authors gratefully acknowledge support from the Italian Space Agency (ASI) through contract I/060/08/0. B. Langlais supported through ANR-08-JCJC-0126. Operations of the Mars Express spacecraft by the European Space Agency (ESA) are gratefully acknowledged.

References

Acuna, M. H.; Connerney, J. E. P.; Ness, N. F.; Lin, R. P.; Mitchell, D.; Carlson, C. W.; McFadden, J.; Anderson, K. A.; Reme, H.; Mazelle, C.; Vignes, D.; Wasilewski, P.; Cloutier, P.: Global Distribution of Crustal Magnetization Discovered by the Mars Global Surveyor MAG/ER Experiment, Science, Vol. 284, Iss. 5415, p. 790 (1999).

Cook C.E., Bernfeld M., Radar Signals, Academic Press, New York, 1967

Espley J. R., Farrell W. M., Brain D. A., Morgan D. D., Cantor B., Plaut J. J., Acuna M. H. and Picardi G. , 2007: Absorption of MARSIS radar signal: Solar energetic particles and the daytime ionosphere, Geophysical Research Letters, Vol. 34.

Gurnett D. A., Huff R. L., Morgan D. D., Persoon A. M., Averkamp T. F., Kirchner D. L., Duru F., Akalin F., Kopf A. J., Nielsen E., Safaeinili A., Plaut J. J. and Picardi G., 2007: An overview of radar soundings of the martian ionosphere from the Mars Express spacecraft, Advances in Space Research 41, 1335-1346.

Ilyushin, Ya. A., and Kunitsyn, V. E. , 2004: Methods for Correcting Ionosphere Distortions of Orbital Ground-Penetrating Radar Signals, Journal of Communications Technology and Electronics, Vol. 49, pp. 154-165.

Langlais, B., V. Lesur, M.E. Purucker, J.E.P. Connerney, and M. Mandea, Crustal magnetic fields of terrestrial planets, Space Science Reviews, 152, doi:10.1007/s11214-009-9557-y, 2010.

Langlais B., M. Purucker, and M. Mandea, Crustal magnetic field of Mars, *J. Geophys. Res.*, 109 (2004), doi 10.1029/2003JE002048.

Leblanc, F., Witasse, O., Lilensten, J., Frahm, R. A., Safaeinili, A., Brain, D. A., Mouginot, J., Nilsson, H., Futaana, Y., Halekas, J., Holmstro¨m, M., Bertaux, J. L., Winningham, J. D., Kofman, W., and Lundin R., Observations of aurorae by SPICAM ultraviolet spectrograph on board Mars Express: Simultaneous ASPERA.3 and MARSIS measurements, Journal of Geophysical Research, 113, (2008) A08311, doi:10.1029/2008JA013033.

Lillis R. J., Frey H. V., Manga M., Mitchell D. L., Lin R. P., Acuna M. H., Bougher S. W.: An improved crustal magnetic field map of Mars from electron reflectometry: Highland volcano magmatic history and the end of the martian dynamo, Icarus 194 (2008) 575-596.

Lillis R. J., Fillingim M. O., Peticolas L. M., Brain D. A., Lin R. P. and Bougher S. W., 2009: Nightside ionosphere of Mars: Modeling the effects of crustal magnetic fields and electron pitch angle distributions on electron impact ionization, Journal of Geophysical Research, 114, E11009.

Lillis, R. J., Brain, D. A., England, S. L., Withers, P., Fillingim, M. O., Safaeinili, A., 2010; Total electron content in the Mars ionosphere: Temporal studies and dependence on solar EUV flux, Journal of Geophysical Research Vol. 115 A11314.

Lillis, R. J., Fillingim, M. O. and Brain D. A., 2011: Three-dimensional structure of the Martian nightside ionosphere:Predicted rates of impact ionization from Mars Global Surveyor magnetometer and electron reflectometer measurements of precipitating electrons, Journal of Geophysical Research, 116, A12317, doi:10.1029/2011JA016982, 2011.

Morgan D. D., Gurnett D. A., Kirchner D. L., Huff R. L., Brain D. A., Boynton W. V., Acuna M. H., Plaut J. J. and Picardi G.: Solar control of radar wave absorption by the Martian ionosphere, Geophysical Research Letters, Vol. 33, 2006.

Mouginot J., Kofman, W., Safaeinili, A., and Herique, A. , 2008: Correction of the ionospheric distortion on the MARSIS surface sounding echoes, Planetary and Space Science, Vol. 56, pp. 917-926.

Němec, F., Morgan, D. D., Gurnett, D. A., and Duru, F., 2010: Nightside ionosphere of Mars: Radar soundings by the Mars Express spacecraft, Journal of Geophysical Research, 115, E12009, doi:10.1029/2010JE003663, 2010.

Němec, F., Morgan, D. D., Gurnett, D. A., and Brain D. A., 2010: Areas of enhanced ionization in the deep nightside ionosphere of Mars, Journal of Geophysical Research, 116, E06006, doi:10.1029/2011JE003804, 2011.

Nielsen E., Zou H., Gurnett D. A. , Kirchner D. L., Morgan D. D., Huff R. , Orosei R. , Safaeinili A. , Plaut J. J. and Picardi G., 2006: Observations of vertical reflections from the topside martian ionosphere, Space Science Reviews (2006) 126: 373–388.

Picardi, G.Sorge, S., 2000:Adaptive compensation of ionosphere dispersion to improve subsurface detection capabilities in low-frequency radar systems. Proc. SPIE Vol. 4084, p. 624-629, Eighth International Conference on Ground Penetrating Radar.

Picardi G., Plaut J. J., Biccari D., Bombaci O., Calabrese D., Cartacci M., et al. , 2005: Radar Soundings of the Subsurface of Mars, Science, Vol. 310, pp. 1925-1928.

Picardi, G., and 14 colleagues 2008: Mars ionosphere data inversion by MARSIS surface and subsurface signals analysis, Radar Conference, 2008. RADAR ’08. IEEE, 1-5, 2008.

Safaeinili, A., Kofman, W., Mouginot, J., Gim, Y., Herique, A., Ivanov, A. B., Plaut, J. J., and Picardi, G. , 2007: Estimation of the total electron content of the Martian ionosphere using radar sounder surface echoes, Geophysical Research Letters, Vol. 34.

Safaeinili, A., Kofman, W., Nouvel, J. F., Herique, A., Jordan, R. L., 2003: Impact of Mars ionosphere on orbital radar sounder operation and data processing, Planetary and Space Science, Volume 51, Issue 7-8, p. 505-515, 2003.

Zhang, Z., Nielsen, E., Plaut, J. J., Orosei, R., and Picardi, G. , 2009: Ionospheric corrections of MARSIS subsurface sounding signals with filters including collision frequency, Planetary and Space Science, Vol. 57, pp. 393-403.

Figure captions

Fig. 1. Simulation of the effect of phase distortion on an ideal radar signal. Blue line: convolution of the ideal reflected "chirp"; blue, black, red and purple lines: convolutions pertaining to the a_1, a_2, a_3, and a_4 expansion terms (see Eqs. A.11 in the appendix - assuming that f_p = 1 MHz and τ_0 = 533μs). All lines have been normalized to their peak values.

Fig. 2. TEC evaluated through the CM at three frequencies (3, 4 and 5 MHz, as red, blue and black lines) versus SEA for orbit 6001 before (2a) and after (2b) the filtering process.

Fig. 3. Comparison, during the night side of orbit 2600, between the CM TEC (dotted blue line) for f_0 = 4 MHz and the TEC obtained by Mouginot et al. (2008) (dotted red line).

Fig. 4. Same comparison as in Fig. 3, but for orbit 2640.

Fig. 5. TEC_{filt}, averaged over 0.1° SEA bins, plotted as a function of SEA, for four different frequencies (1.8, 3, 4 and 5 MHz correspond to purple, blue, red and black dots, respectively). The Chapman model TEC is represented by the blue solid line.

Fig. 6: TEC 0.1° bin averages for f_0= 4 MHz, calculated for five different years during the night-side (6a) and day-side (6b).

Fig. 7. Filtered 4 MHz TEC values (blue), their fit function (purple) and ΔTEC (black) for orbit 6001.

Fig. 8. Latitude-longitude maps of ΔTEC_{pc}. The latitudes range from -90° to 54°, as above 54° no ΔTEC values could be deduced from MARSIS data.

Fig. 9. Latitude-longitude maps of ΔTEC_{pc} (9a) and α (9b). α is the angle between the ambient magnetic field vector of internal origin, predicted by an ESD model, and the local vertical direction. The latitudes range from -90° to 54°, as above 54° no TEC values could be deduced from MARSIS data. Red dotted (yellow dashed) lines highlight quasi vertical (horizontal) field regions.

Fig. 10. Maps of α (left panel) and ΔTEC_pc(right panel) for the -65.5°/-7.5° latitude range (vertical axis) and for the 104°/194° longitude range (horizontal axis). Red dotted (yellow dashed) lines highlight quasi vertical (horizontal) field regions.

Fig. 11. Panel a: histograms (each normalized to its peak value) of ΔTEC_pc for nearly vertical magnetic field (80°-90°, dotted cityscape, peak value 1793) and nearly horizontal magnetic field (0°-10°, solid cityscape, peak value 278). Panels b and c: ΔTEC_pc histograms (also normalized to peak values) for nearly vertical and nearly horizontal magnetic field (coded as in panel a) for data pertaining to region 1 (R1) and to region 2 (R2) of Fig. 9 (see text for details and Fig. 10 for R1). Peak values are: 60 (solid line) and 290 (dotted line) for panel b; 45 (solid line) and 20 (dotted line) for panel c. Panel d: histograms of total magnetic field intensity for region 2 (dotted cityscape, 1464 bins) and for region 1 (solid cityscape, 5278 bins, some of which not plotted as the abscissa is limited to 500 nT).

Fig. 12. Top panel: number of cases for 5 nT bins of B. Bottom panel: averages of ΔTEC_pc for 5 nT bins of B.

Fig. 13. Top panel: histogram of α average values for the 51120 1°x1° pixels of Fig. 9b, binned in α bins of 5° between 0 and 90°. Bottom panel, averages of ΔTEC_{pc} (see Fig. 8), calculated over α bins of 5° between 0 and 90°.

Fig. A.1. Reflected power as a function of time during frame 84 of orbit 10741. The red line shows the uncorrected received signal; the blue line shows the reflected power after correction through the Contrast Method.

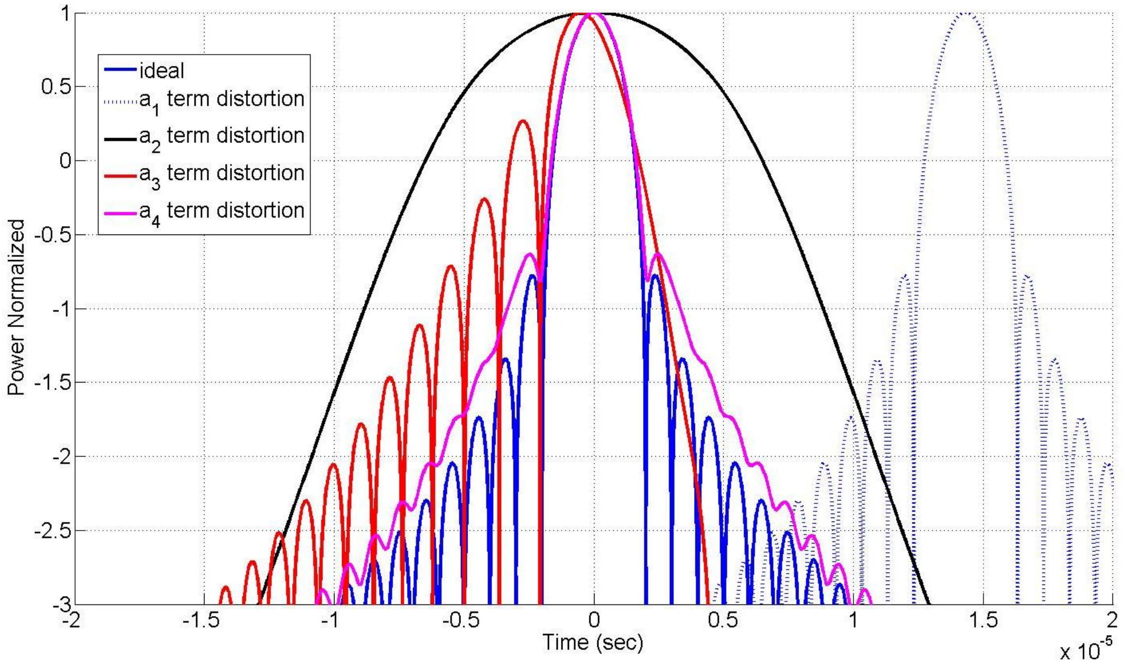

Fig. 1. Simulation of the effect of phase distortion on an ideal radar signal. Blue line: convolution of the ideal reflected "chirp"; blue, black, red and purple lines: convolutions pertaining to the a_1, a_2, a_3, and a_4 expansion terms (see Eqs. A.11 in the appendix - assuming that f_p = 1 MHz and τ_0 = 533 µs). All lines have been normalized to their peak values.

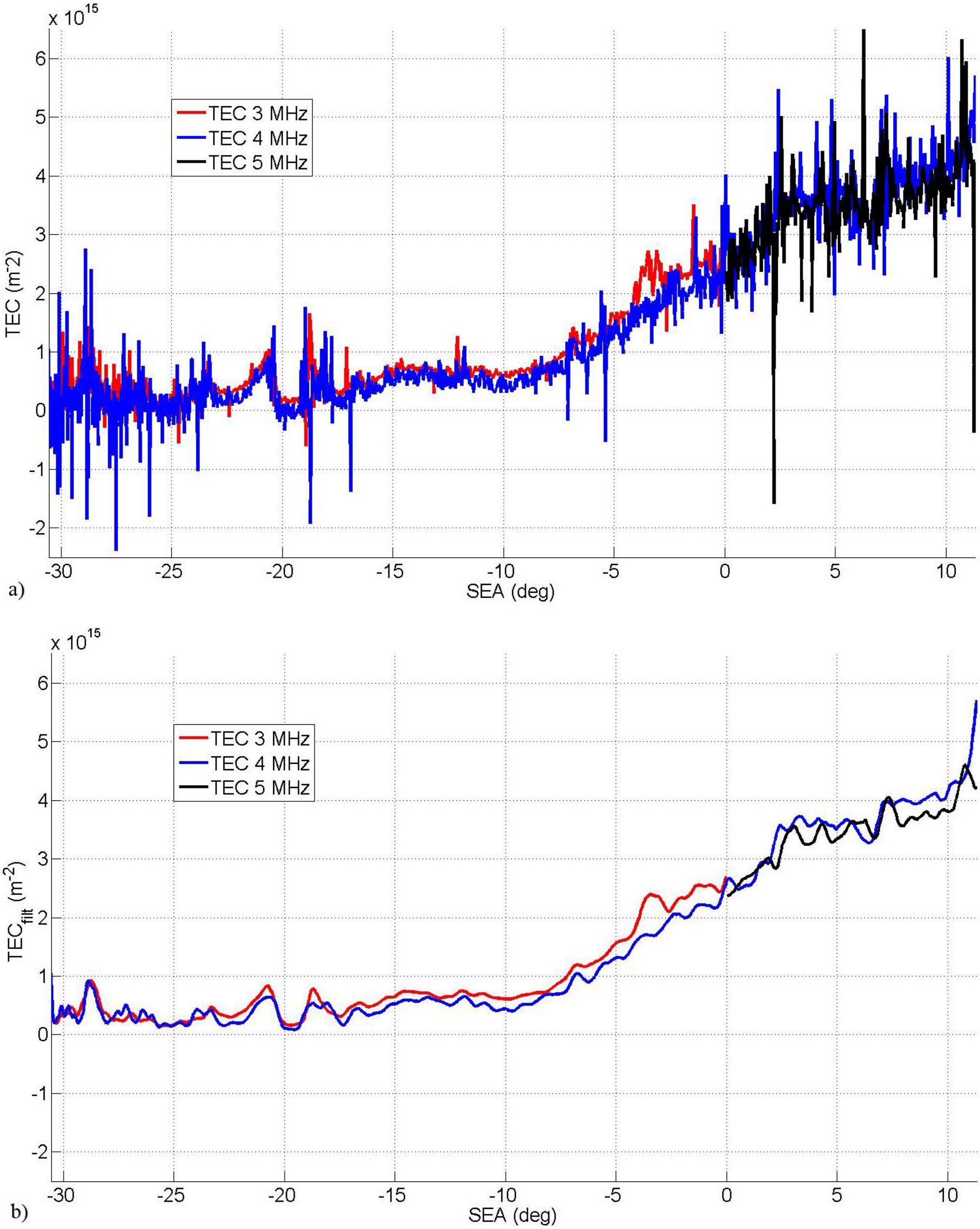

Fig. 2. TEC evaluated through the CM at three frequencies (3, 4 and 5 MHz, as red, blue and black lines) versus SEA for orbit 6001 before (3a) and after (3b) the filtering process.

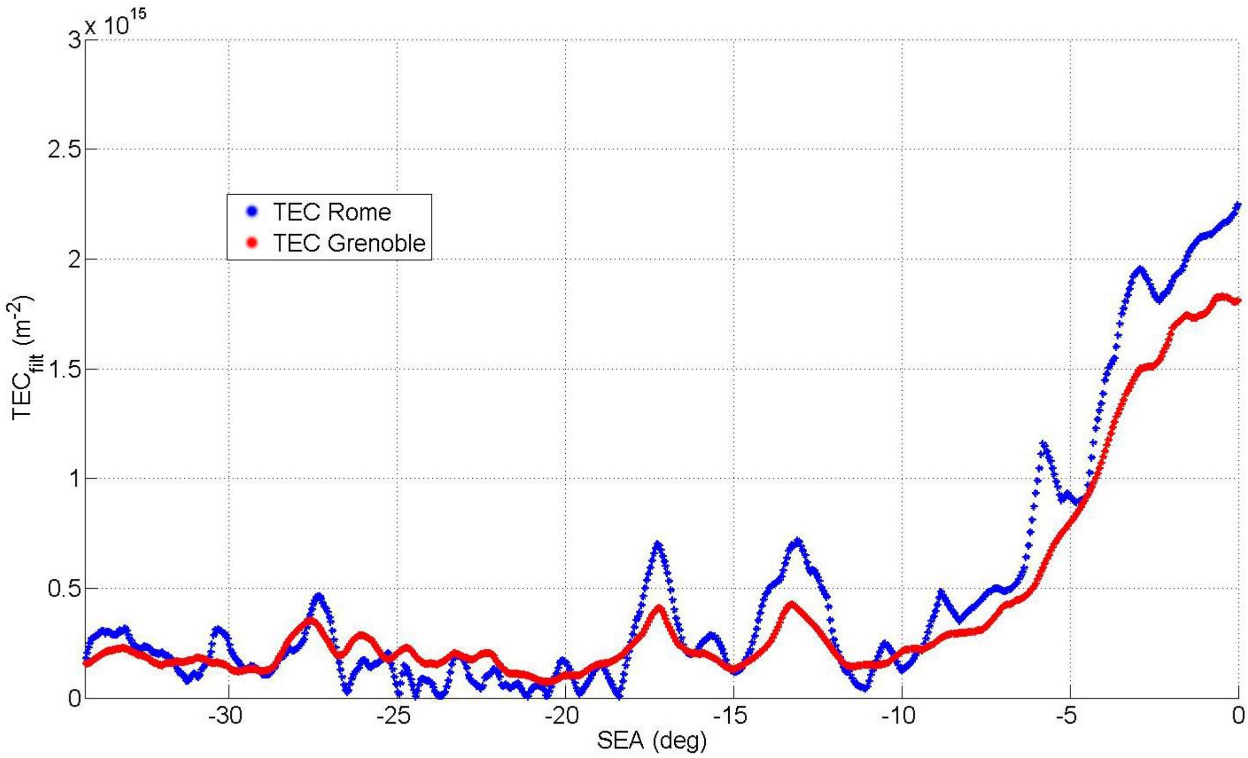

Fig. 3. Comparison, during the night side of orbit 2600, between the CM TEC_{filt} (dotted blue line) for f_0 = 4 MHz and the TEC obtained by Mouginot et al. (2008) (dotted red line). The Mouginot TEC data were downloaded from the ESA ftp server (ftp://psa.esac.esa.int/pub/mirror/MARS-EXPRESS) and were filtered in the same way as the CM TEC.

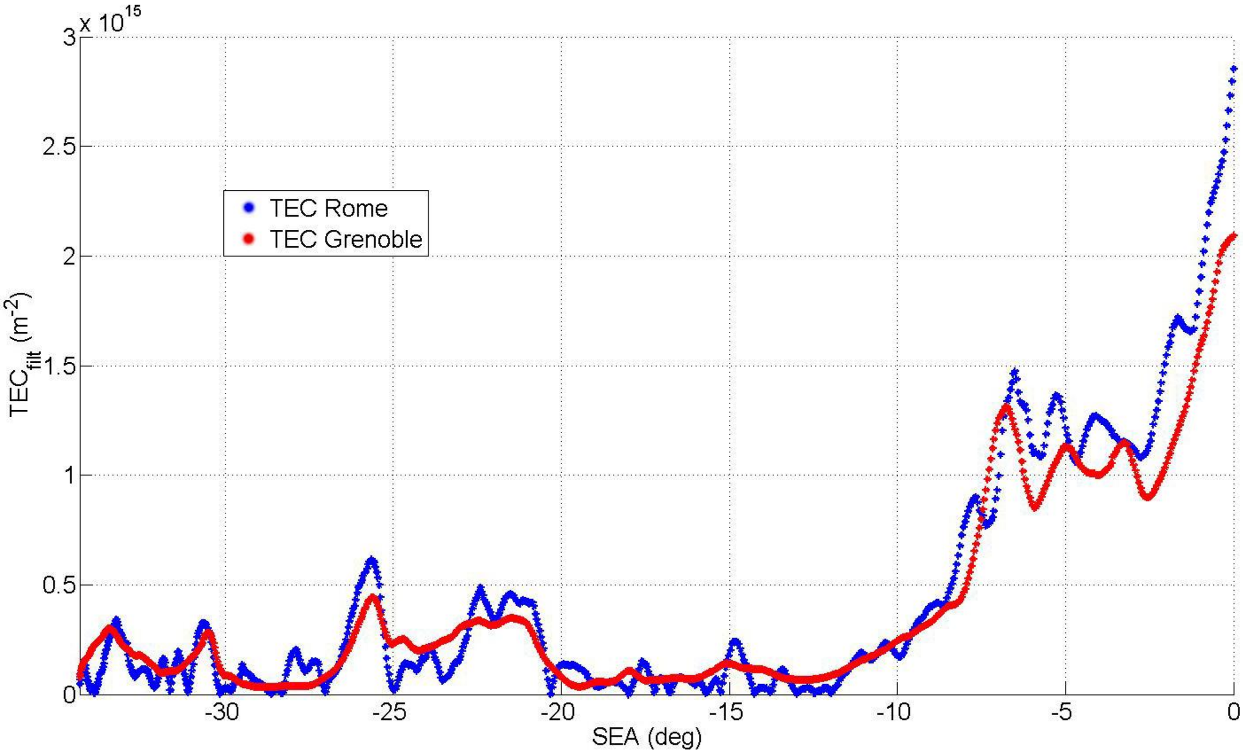

Fig. 4. Same comparison as in Fig. 3, but for orbit 2640.

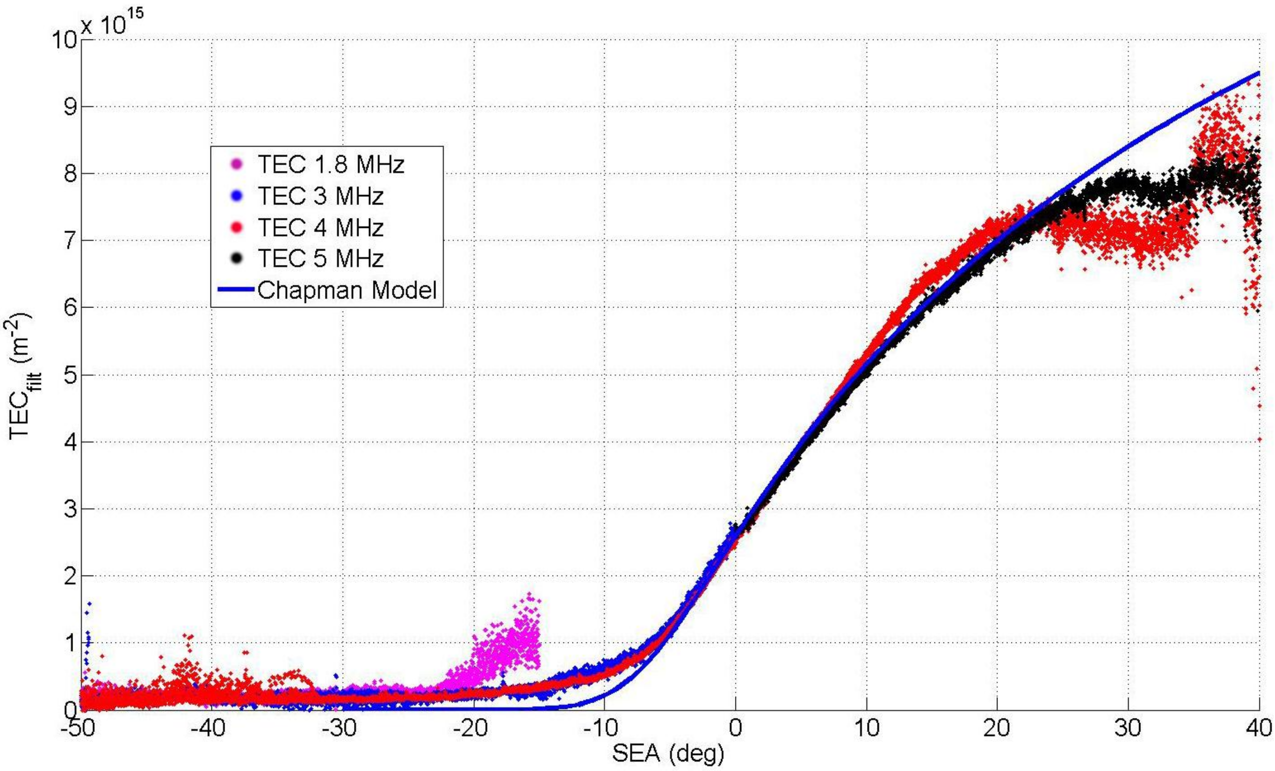

Fig. 5. TEC_{filt}, averaged over 0.1° SEA bins, plotted as a function of SEA, for four different frequencies (1.8, 3, 4 and 5 MHz).The blue solid line displays the TEC calculated from the Chapman model (see text for more details).

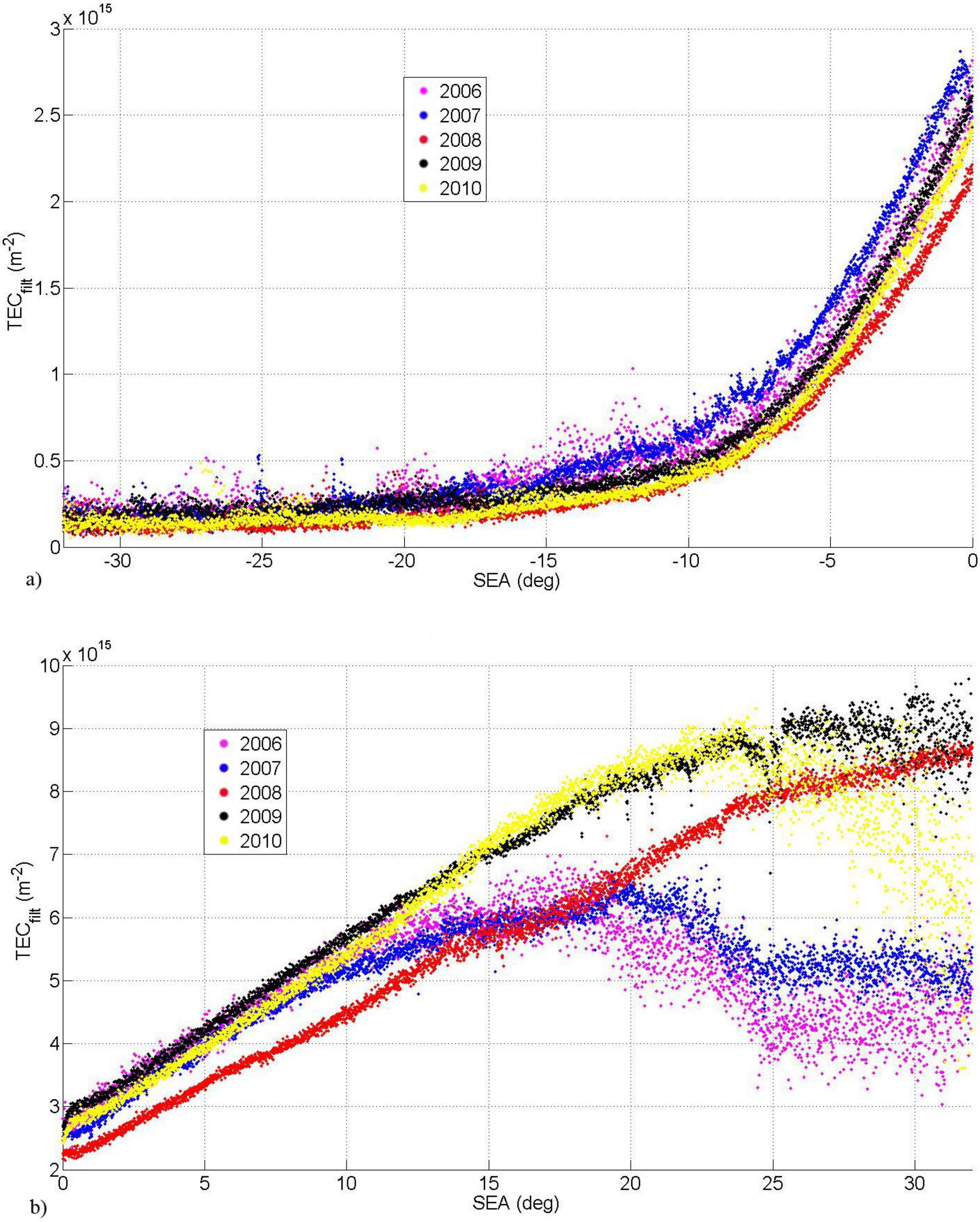

Fig. 6. TEC 0.1° bin averages for f_0= 4 MHz, calculated for five different years during the night-side (a) and day-side (b).

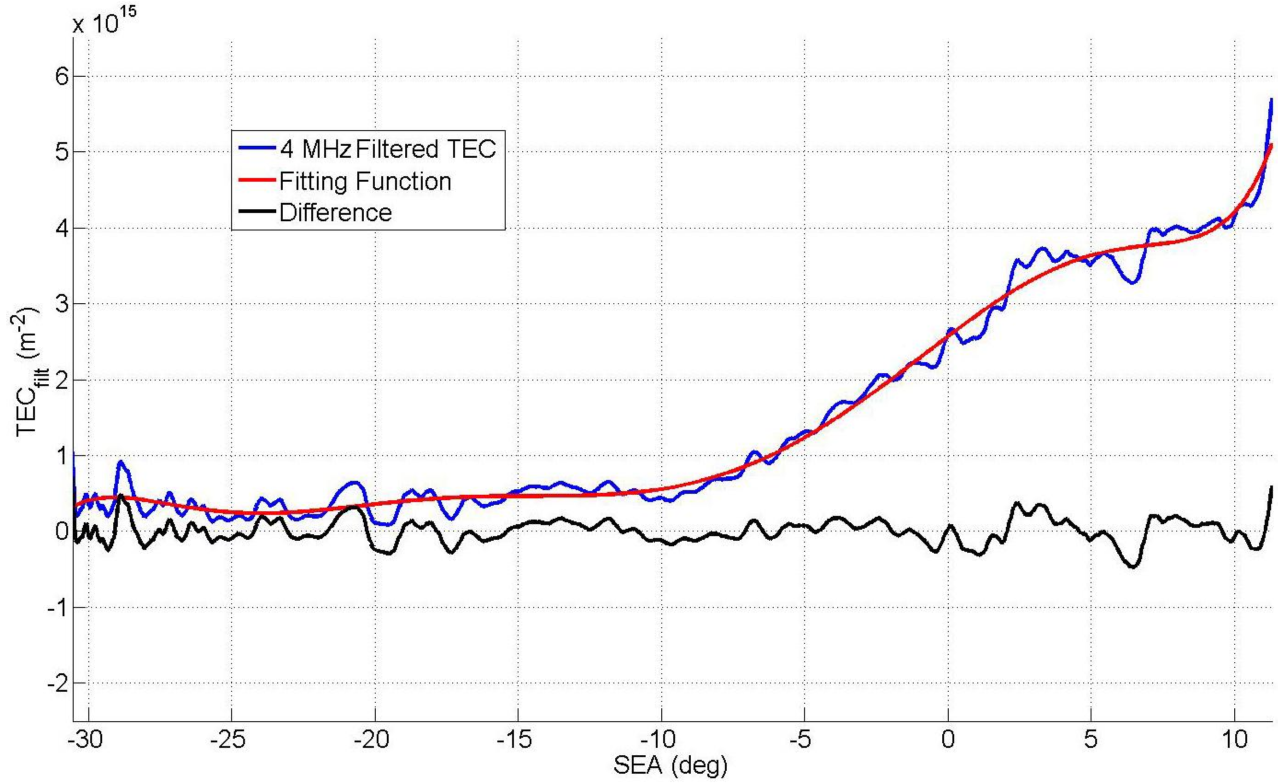

Fig. 7. Filtered 4 MHz TEC values (blue), their fit function (purple) and ΔTEC (black) for orbit 6001.

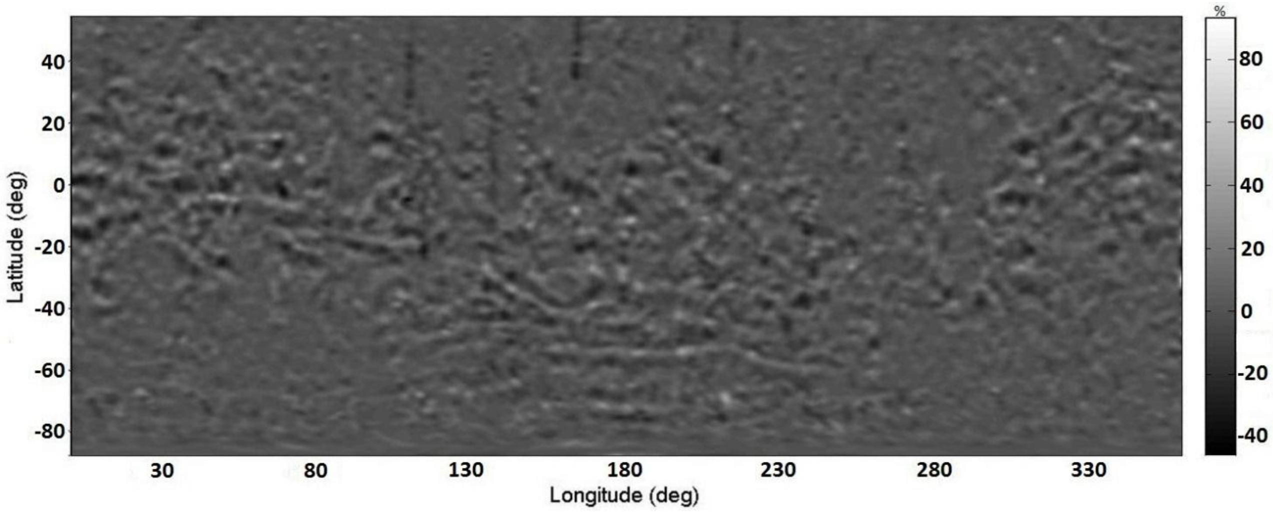

Fig. 8. Latitude-longitude maps of ΔTEC_{pc}. The latitudes range from -90° to 54°, as above 54° no ΔTEC values could be deduced from MARSIS data.

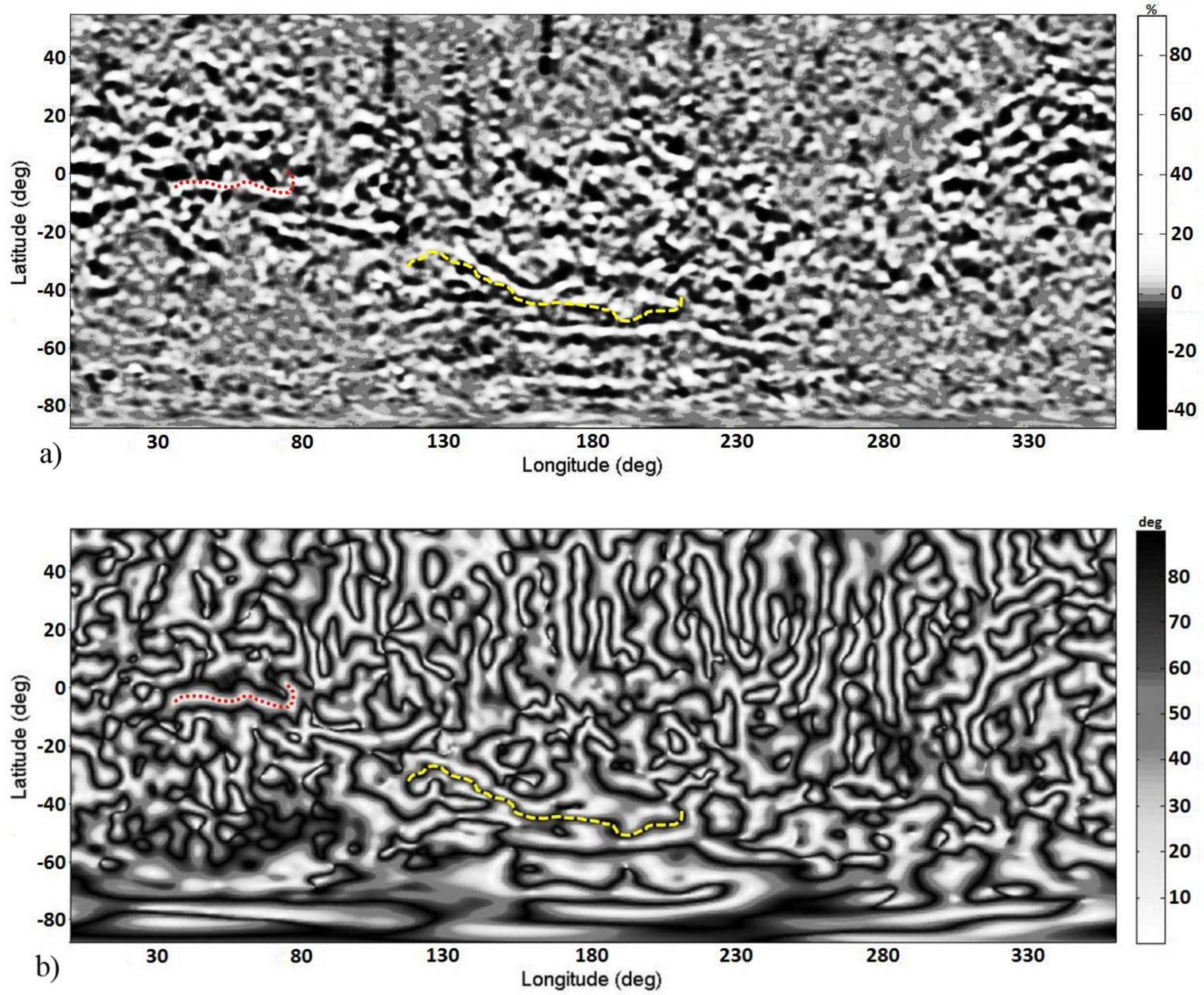

Fig. 9. Latitude-longitude maps of ΔTEC_{pc} (9a) and α (9b). α is the angle between the ambient magnetic field vector of internal origin, predicted by an ESD model, and the local vertical direction. The latitudes range from -90° to 54°, as above 54° no TEC values could be deduced from MARSIS data. Red dotted (yellow dashed) lines highlight quasi vertical (horizontal) field regions.

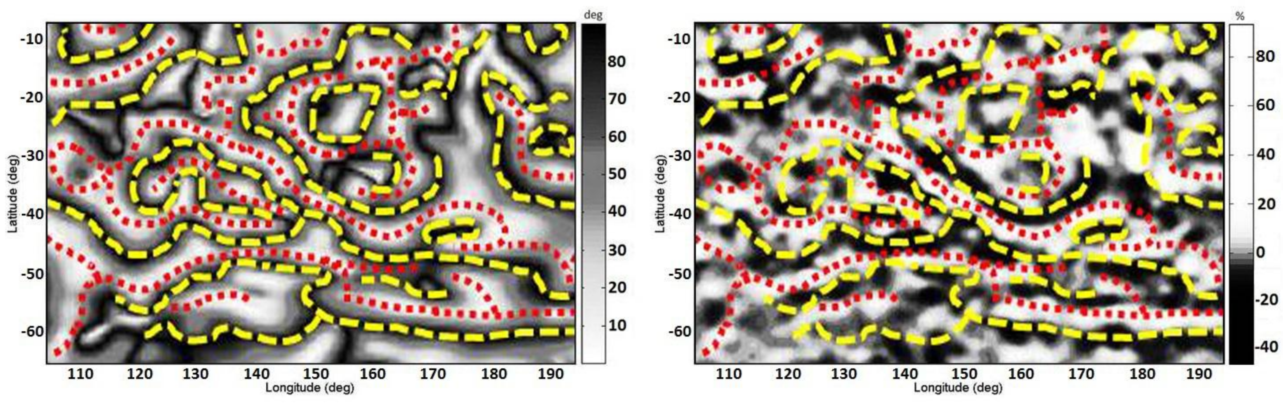

Fig. 10. Maps of α (left panel) and ΔTEC_pc(right panel) for the -65.5°/-7.5° latitude range (vertical axis) and for the 104°/194° longitude range (horizontal axis). Red dotted (yellow dashed) lines highlight quasi vertical (horizontal) field regions.

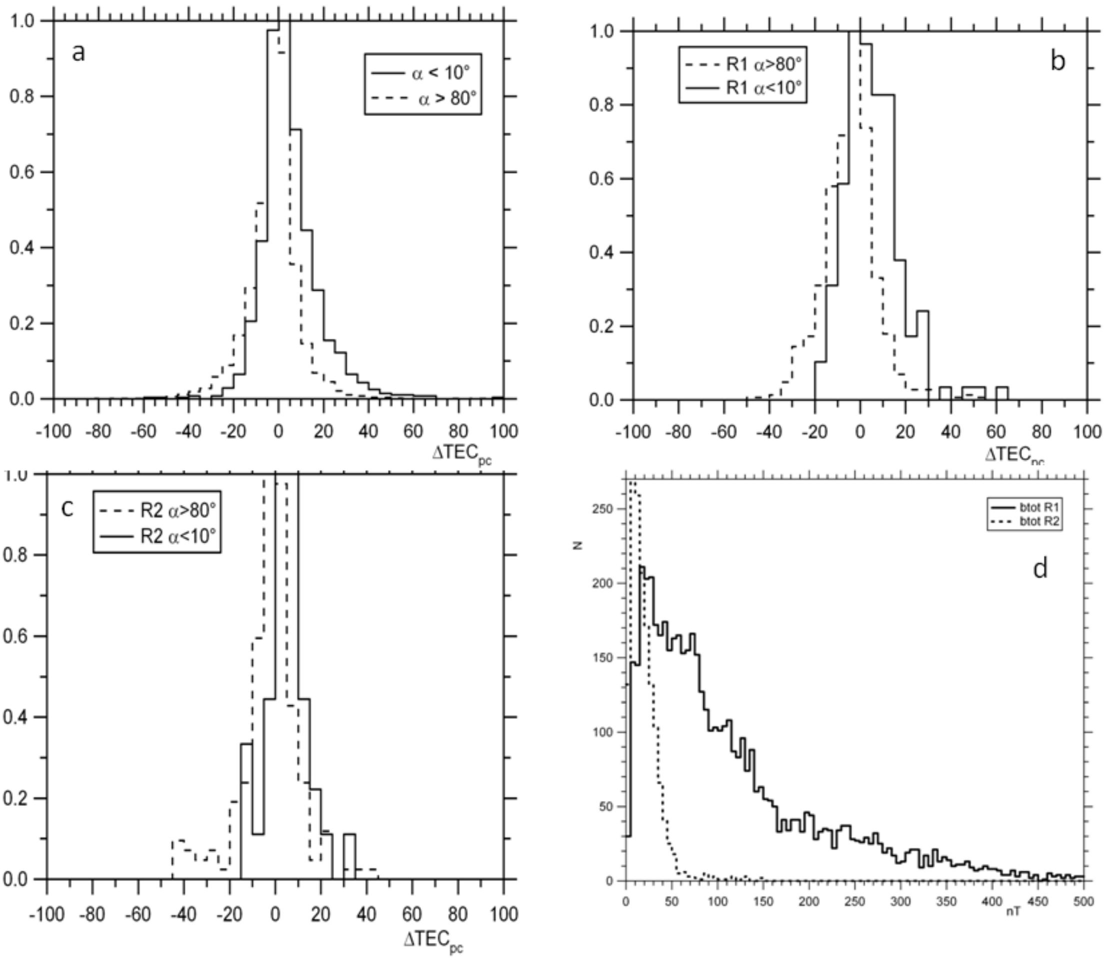

Fig. 11. Panel a: histograms (each normalized to its peak value) of ΔTEC_pc for nearly horizontal magnetic field (80°-90°, dotted cityscape, peak value 1793) and nearly vertical magnetic field (0°-10°, solid cityscape, peak value 278). Panels b and c: ΔTEC_pc histograms (also normalized to peak values) for nearly vertical and nearly horizontal magnetic field (coded as in panel a) for data pertaining to region 1 (R1) and to region 2 (R2) of Fig. 9 (see text for details and Fig.10 for R1). Peak values are: 60 (solid line) and 290 (dotted line) for panel b; 45 (solid line) and 20 (dotted line) for panel c. Panel d: histograms of total magnetic field intensity for region 2 (dotted cityscape, 1464 bins) and for region 1 (solid cityscape, 5278 bins, some of which not plotted as the abscissa is limited to 500 nT).

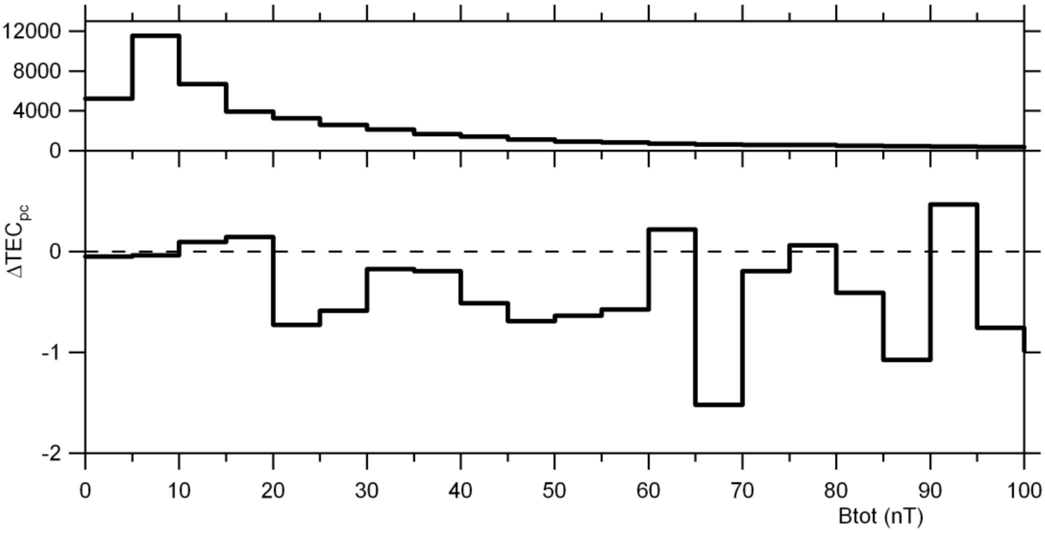

Fig. 12. Top panel: number of cases for 5 nT bins of B. Bottom panel: averages of ΔTEC_pc for 5 nT bins of B.

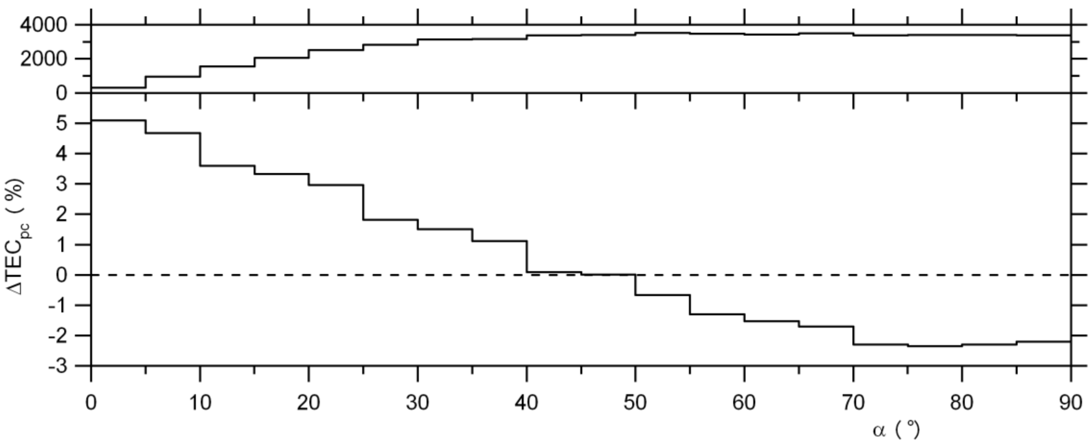

Fig. 13. Top panel: histogram of α average values for the 51120 1°x1° pixels of Fig. 9b, binned in α bins of 5° between 0 and 90°. Bottom panel, averages of ΔTEC_{pc} (see Fig. 8), calculated over α bins of 5° between 0 and 90°.

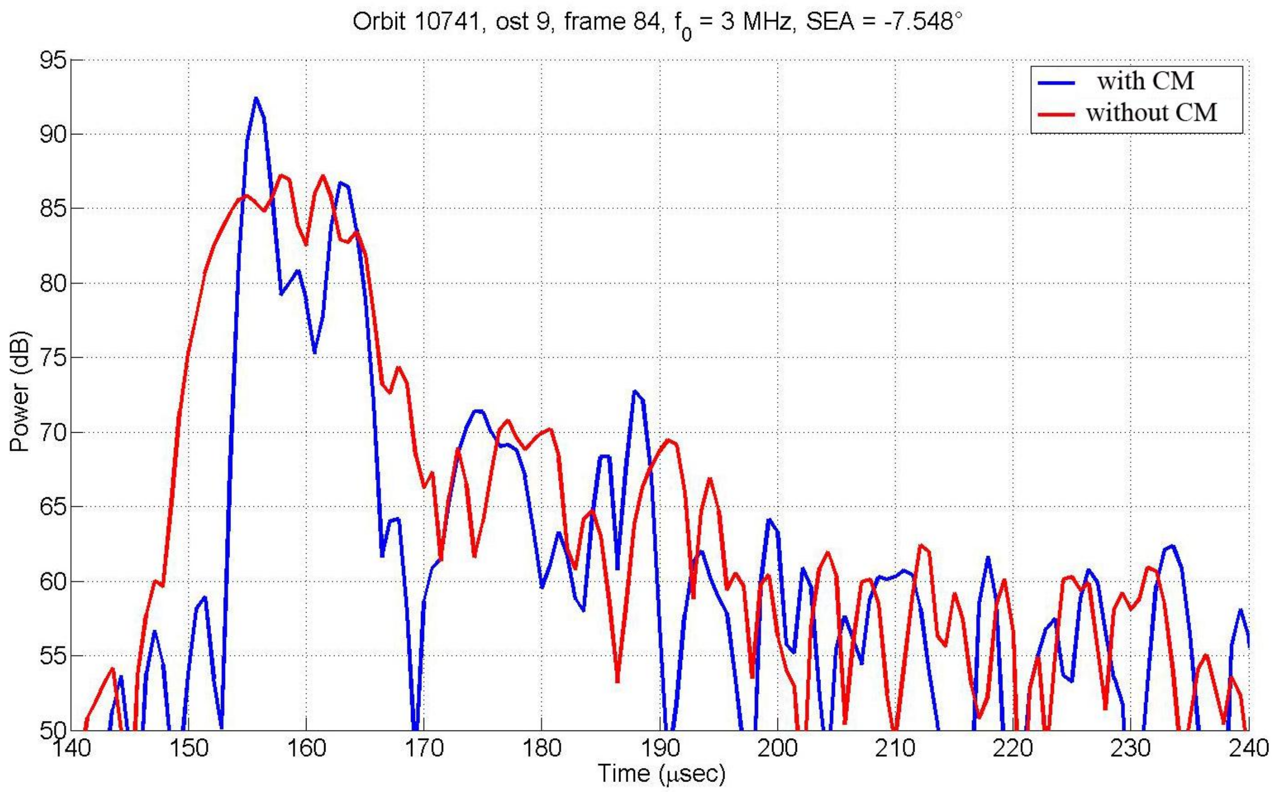

Fig. A.1. Reflected power as a function of time during frame 84 of orbit 10741. The red line shows the uncorrected received signal; the blue line shows the reflected power after correction through the Contrast Method.